Chapter 1

Fluid–Structure Interaction (FSI) Methods for the Navier–Stokes Equations

Anastasios C. Felias[a]

Department of Medicine, University of Ioannina, Ioannina, 45110, Epirus, Greece

Konstantina C. Kyriakoudi[b]

Department of Mathematics, University of Ioannina, Ioannina, 45110, Epirus, Greece

Michail Th. Rassias[c]

Department of Mathematics and Engineering Sciences, Hellenic Military Academy, 16673, Attiki, Greece

Michail A. Xenos[b],
mxenos@uoi.gr *

Contents

*Correspondence email

Abstract: Advanced fluid–structure interaction (FSI) simulations, exploiting the dynamic interaction between the vessel hemodynamics and wall deformation, is conducted to simulate the biomechanical behaviour of arterial vessels. Initially, in this chapter a brief description of the basic fluid equations is introduced. Additionally, analytical solutions of basic fluid mechanics problems are discussed. Main focus is set on applying two–dimensional FSI methods on the Navier–Stokes equations, mathematically modelling blood flow in arteries. The cardiovascular data obtained are compared with numerical results, derived from numerical methods. In the FSI approach, the initial two–dimensional fluid equations are expanded to a mixed Euler–Lagrange formulation to study blood flow during the entire cardiac cycle. Transport equations are transformed into a moving body–fitted reference frame using generalised curvilinear coordinates. Furthermore, a generalization to a three–dimensional FSI approach is introduced and discussed.

MSC: 65M08, 65N08, 35Q30

The Navier–Stokes Equations in Fluid Dynamics

1. Navier–Stokes equations

The Navier–Stokes equations are PDEs that model the motion of practically every fluid, with examples ranging from, microscale, in microfluidic devices, to mesoscale, such as the blood flow inside the human body, to the macroscale, such as the formation of stars. Forces acting on the fluid include the pressure $p(\mathbf{x}, t)$, the kinematic viscosity ν and a defined external force field $\mathbf{F}(\mathbf{x}, t)$ acting on the fluid, such as the gravitational field. The Navier–Stokes equations are the result of the Newton's second law for the fluid flow, with respect to these forces, in terms of partial derivatives of the velocity $\mathbf{q}(\mathbf{x}, t)$ of the fluid as a function of position $\mathbf{x}$ and time t. The Navier–Stokes system, for an incompressible fluid, is given as,[2,10]

$$\begin{cases} \nabla_{\mathbf{x}} \cdot \mathbf{q} = 0, \\ \underbrace{\mathbf{q}_t + (\mathbf{q} \cdot \nabla_{\mathbf{x}})\mathbf{q}}_{inertia\ terms} = \underbrace{-\dfrac{\nabla_{\mathbf{x}} p}{\rho} + \nu \Delta_{\mathbf{x}} \mathbf{q} + \mathbf{F}}_{force\ terms} \end{cases} \tag{1}$$

where more specifically,

- $\mathbf{q}_t$: local acceleration.
- $(\mathbf{q} \cdot \nabla_{\mathbf{x}})\mathbf{q}$: nonlinear translational acceleration.
- $-\dfrac{\nabla_{\mathbf{x}} p}{\rho}$: internal forcing term (internal source).
- $\nu \Delta_{\mathbf{x}} \mathbf{q}$: diffusion terms.
- $\mathbf{F}$: external forcing term (external source).

The first equation of the system is the continuity equation (mass conservation) and the second, vector, equation is the momentum equation, in apparent analogy with Newton's 2nd law. Usually, with respect to the spatial variables $\mathbf{x}$, we work on $\mathbb{R}^2$ or $\mathbb{R}^3$. As an illustration, in the case of a three-dimensional and fully developed flow, in Cartesian coordinates, with $\mathbf{q} = (u, v, w)$ and $\mathbf{x} = (x, y, z)$, the reduced

form of (1) is,

$$\begin{cases} u_x + v_y + w_z = 0, \\ u_t + uu_x + vu_y + wu_z = -\dfrac{p_x}{\rho} + \nu(u_{xx} + u_{yy} + u_{zz}) + F_1, \\ v_t + uv_x + vv_y + wv_z = -\dfrac{p_y}{\rho} + \nu(v_{xx} + v_{yy} + v_{zz}) + F_2, \\ w_t + uw_x + vw_y + ww_z = -\dfrac{p_z}{\rho} + \nu(w_{xx} + w_{yy} + w_{zz}) + F_3 \end{cases} \tag{2}$$

It should be emphasized that we can express the Navier–Stokes equations in any curvilinear coordinate system by substituting the particular form of the gradient vector, obtained by chain differentiation. The Navier–Stokes system of equations is of order 2 in space and of order 1 in time, nonlinear and, in the general case, inhomogeneous. It is furthermore coupled, since none of the equations can be solved independently of the other. These equations are connected to one of the famous Millennium Problems.[4]

The difficulty in solving the problem lies in the underlying concept of nonlinear advection, which makes the equations extremely sensitive to initial conditions, being the main reason why the conjectures of the Millennium problem are so difficult. Further contributing to the difficulty of solution is the fact that the solutions involve turbulence, an area of fluid dynamics that is not well understood.[4] Nevertheless, the equations can be solved under appropriate assumptions about the flow. Moreover, the Navier–Stokes problem, in two dimensions, was studied in the 1960s, through the existence of everywhere certain and smooth solutions.[4,10] The equations, coupled with the Maxwell equations, serve a key role in magnetohydrodynamics.

1.1. *The Euler equations*

In the case where the viscous character of the flow can be considered negligible, the Navier–Stokes momentum equation is reduced to the Euler equation,

$$\mathbf{q}_t + (\mathbf{q} \cdot \nabla_{\mathbf{x}})\mathbf{q} = -\frac{\nabla_{\mathbf{x}} p}{\rho} + \mathbf{F} \tag{3}$$

Suppose we are interested in the case of steady and incompressible flow. Assuming that the force field is conservative, i.e., that there exists $V : \mathbf{F} = \nabla_{\mathbf{x}} V$, and that

the flow is unsteady, $\nabla_{\mathbf{x}} \times \mathbf{q} = \mathbf{0}$, we obtain,

$$\begin{aligned}
(\mathbf{q}\cdot\nabla_{\mathbf{x}})\mathbf{q} &= \nabla_{\mathbf{x}}\left(-\frac{p}{\rho}\right) + \nabla_{\mathbf{x}} V \\
\Leftrightarrow\ \nabla_{\mathbf{x}}\left(\frac{1}{2}\mathbf{q}\cdot\mathbf{q}\right) &= \nabla_{\mathbf{x}}\left(-\frac{p}{\rho} + V\right) \\
\Leftrightarrow\ \nabla_{\mathbf{x}}\left(\frac{1}{2}|\mathbf{q}|^2 + \frac{p}{\rho} - V\right) &= 0 \\
\Leftrightarrow \frac{1}{2}|\mathbf{q}|^2 + \frac{p}{\rho} - V &= C : const
\end{aligned} \tag{4}$$

Here, (4) is a solution of the Euler equation and is called the Bernoulli equation. Note that, to arrive at (4), we exploited the relation,

$$\nabla_{\mathbf{x}}\left(\frac{1}{2}\mathbf{q}\cdot\mathbf{q}\right) = \mathbf{q}\times(\underbrace{\nabla_{\mathbf{x}}\times\mathbf{q}}_{=\mathbf{0}}) + (\mathbf{q}\cdot\nabla_{\mathbf{x}})\mathbf{q} \tag{5}$$

In the one–dimensional case, in the absence of forcing terms, the Euler momentum equation reduces to the Burgers inviscid equation, the study of which gives important insights into the Euler momentum equation.

1.2. *Dimensionalization & Reynolds number*

We consider the Navier–Stokes equations, (1), in the absence of an external force, where the goal is to express their dimensionless form. For this purpose we consider characteristic length L and velocity U, so that the new, dimensionless, variables are expressed via the transformation,

$$\begin{cases}
\mathbf{x}^* := \dfrac{\mathbf{x}}{L}, \nabla^* := L\nabla_{\mathbf{x}}, \\[2ex]
\mathbf{q}^* := \dfrac{\mathbf{q}}{U}, \\[2ex]
t^* := \dfrac{t}{\frac{L}{U}}
\end{cases} \tag{6}$$

With respect to the pressure p there is no natural choice, and depending on the type of flow we get different dimensionless pressures, as,

$$\begin{cases}
p^* = \dfrac{p}{\rho U^2} \text{ (high velocity flows)}, \\[2ex]
p^* = \dfrac{pL}{\mu U} \text{ (Stokes creeping flows)}
\end{cases} \tag{7}$$

Thus, substituting (6) and (7) into the equations (1), for high-speed flows, we obtain,

$$\begin{cases}
\nabla^*\cdot\mathbf{q}^* = 0, \\[2ex]
\dfrac{\partial\mathbf{q}^*}{\partial t^*} + (\mathbf{q}^*\cdot\nabla^*)\mathbf{q}^* = -\nabla^* p^* + \dfrac{\nu}{LU}\nabla^{*2}\mathbf{q}^*
\end{cases} \tag{8}$$

while for slow, viscous-dominated flows,

$$\begin{cases} \nabla^* \cdot \mathbf{q}^* = 0, \\ \\ \dfrac{LU}{\nu}\left(\dfrac{\partial \mathbf{q}^*}{\partial t^*} + (\mathbf{q}^* \cdot \nabla^*)\mathbf{q}^*\right) = -\nabla^* p^* + \nabla^{*2}\mathbf{q}^* \end{cases} \tag{9}$$

Definition 1. [20] The dimensionless number,

$$Re := \frac{LU}{\nu} \tag{10}$$

is called the Reynolds number and makes an important contribution to the prediction of the flow in different states, expressing the ratio between the inertia and viscous forces.

- In the case of high Re, $Re \to \infty$, the momentum equations (8) are reduced to the Euler equations, with the inertia forces dominating the viscous forces, with the term $\frac{1}{Re}\nabla^{*2}\mathbf{q}^*$ being negligible and the fluid behaving as an ideal one.
- In contrast, in the case of low Re, $Re \to 0^+$, the momentum equations (9) describe creeping (or slow) Stokes flows, where viscous forces are dominant. It is worth pointing out that these equations are linear, and there are numerous ways to solve them, e.g. via the Green's (Stokeslet)[9] functions.
- At low Re, flows tend to be laminar, while at high Re, flows tend to be turbulent. Turbulence results from differences in flow velocity and direction, which may cross or even move in the opposite direction to the general direction of the flow, in eddy currents. These eddy currents begin to swirl the flow, consuming energy.
- The Reynolds number has wide applications, ranging from the flow in a pipe (simulating blood flow) to the passage of air over an aircraft wing.

1.3. *Closed – conservative form of the equations*

Our goal now is to derive a closed, conservative form of the equations (2), which is convenient enough for numerical treatment of the equations.[20] We thus consider, without loss of generality, first the left-hand side of the $x-$momentum equation, for which we obtain,

$$\begin{aligned} u_t + uu_x + vu_y + wu_z &= u_t + uu_x + vu_y + wu_z + u \underbrace{(u_x + v_y + w_z)}_{=0 \ (continuity\ equation)} \\ &= u_t + (u^2)_x + (uv)_y + (uw)_z \end{aligned} \tag{11}$$

Regarding the right-hand side, we obtain,

$$-\frac{p_x}{\rho} + \nu(u_{xx} + u_{yy} + u_{zz}) = \left(-\frac{p}{\rho}\right)_x + [(\nu u)_{xx} + (\nu u)_{yy} + (\nu u)_{zz}] \tag{12}$$

Therefore, by combining (11) and (12), the $x-$momentum equation is written,

$$u_t + (u^2)_x + (uv)_y + (uw)_z = \left(-\frac{p}{\rho}\right)_x + [(\nu u)_{xx} + (\nu u)_{yy} + (\nu u)_{zz}] \tag{13}$$

The y- and z–momentum equations are expressed in a similar manner.

1.4. *The Vorticity equation*

As we presented earlier, the Navier–Stokes equations are a coupled system in terms of the velocity field and the flow pressure. We will now provide a way of eliminating the pressure from the equations. For this purpose, we consider the vorticity of both members of the momentum equation of (1), in order to derive an equation for the vorticity $\omega = \nabla_{\mathbf{x}} \times \mathbf{q}$. The driving idea here is that the vorticity of a gradient, such as pressure, is zero, and therefore pressure, or any other conservative quantity, is eliminated from the equation. Under this framework, we get,

$$\begin{aligned}
&\nabla_{\mathbf{x}} \times [\mathbf{q}_t + (\mathbf{q}\cdot\nabla_{\mathbf{x}})\mathbf{q}] = \nabla_{\mathbf{x}} \times \left[-\frac{\nabla_{\mathbf{x}} p}{\rho} + \nu\Delta_{\mathbf{x}}\mathbf{q} + \mathbf{F}\right] \\
\Leftrightarrow\ &(\nabla_{\mathbf{x}} \times \mathbf{q})_t + \nabla_{\mathbf{x}} \times [(\mathbf{q}\cdot\nabla_{\mathbf{x}})\mathbf{q}] = -\underbrace{\frac{\nabla_{\mathbf{x}} \times \nabla_{\mathbf{x}} p}{\rho}}_{=\mathbf{0}} + \nu\nabla_{\mathbf{x}} \times \Delta_{\mathbf{x}}\mathbf{q} + \nabla_{\mathbf{x}} \times \mathbf{F} \\
\Leftrightarrow\ &\omega_t + \nabla_{\mathbf{x}} \times [(\mathbf{q}\cdot\nabla_{\mathbf{x}})\mathbf{q}] = \nu\Delta_{\mathbf{x}}\omega + \nabla_{\mathbf{x}} \times \mathbf{F}
\end{aligned} \tag{14}$$

For the quantity $\nabla_{\mathbf{x}} \times [(\mathbf{q}\cdot\nabla_{\mathbf{x}})\mathbf{q}]$, from (5), we obtain,

$$\nabla_{\mathbf{x}} \times [(\mathbf{q}\cdot\nabla_{\mathbf{x}})\mathbf{q}] = \nabla_{\mathbf{x}} \times (\omega \times \mathbf{q}) \tag{15}$$

Therefore, from (14) and (15), we obtain,

$$\omega_t + \nabla_{\mathbf{x}} \times (\omega \times \mathbf{q}) = \nu\Delta_{\mathbf{x}}\omega + \nabla_{\mathbf{x}} \times \mathbf{F} \tag{16}$$

Moreover, in the case where the external force field is conservative, e.g. it is the Earth's gravitational field $\mathbf{g}$, then (16) becomes,

$$\omega_t + \nabla_{\mathbf{x}} \times (\omega \times \mathbf{q}) = \nu\Delta_{\mathbf{x}}\omega \tag{17}$$

In the case of two–dimensional flow, introducing the stream function,

$$\Big\{ u = \Psi_y,\ v = -\Psi_x \tag{18}$$

the continuity equation is automatically satisfied and (17) is reduced to,

$$(\Delta_{\mathbf{x}}\Psi)_t + \Psi_y(\Delta_{\mathbf{x}}\Psi)_x - \Psi_x(\Delta_{\mathbf{x}}\Psi)_y = \nu\Delta_{\mathbf{x}}(\Delta_{\mathbf{x}}\Psi) \tag{19}$$

The last equation, together with appropriate boundary conditions, describes the two–dimensional fluid flow, taking only the kinematic viscosity as a parameter. Note that the equation for Stokes creeping flow is obtained when the left–hand side of the above equation is assumed to be zero.

2. Analytical solutions

The Navier–Stokes equations, as we have already seen, are a highly intractable PDE system, for which finding analytical solutions requires the adoption of appropriate simplifying assumptions. The presented analytical solutions can serve as exact models in testing numerical solvers.

2.1. *The Couette flow*

Regarding the Couette flow, we consider a steady, incompressible, viscous and two-dimensional flow, between two flat plates, one of which is stationary and the other is moving with constant velocity U, in the $y-$direction. We further assume that both the flow and the pressure gradient exist only in the $y-$direction, i.e. that $\mathbf{q} = (0, v(x, y), 0)$, and that $\nabla p = (0, p_y, 0) = const$. Finally, we assume that the effects of external forces are negligible.

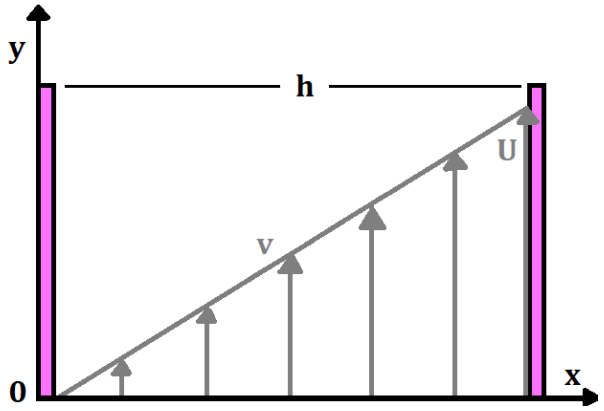

Fig. 1.: Incompressible, viscous flow between two flat plates, with the lower plate held stationary and the upper plate moving at a constant velocity U, in the $y-$direction. As we will see, this graph corresponds to the case of no pressure gradient.

Under the above assumptions, the Navier–Stokes equations are reduced to the ODE,

$$v''(x) = \frac{1}{\mu} p'(y) \tag{20}$$

which, due to the setup of the problem, is accompanied by the boundary conditions,

$$\begin{cases} v(0) = 0, \\ v(h) = U \end{cases} \tag{21}$$

The solution of (20) is easily given, via two successive integrations with respect to x, as,

$$v(x) = \frac{Ux}{h} + \frac{x(x-h)p'(y)}{2\mu} \tag{22}$$

Summarizing now, about Couette flow, we can say the following.

- In the case where the two plates are stationary, i.e. $U = 0$, but there is a pressure gradient, the flow profile is parabolic. For a negative (favorable) pressure gradient, the motion is in the positive $y-$direction, while for a positive (backward) pressure gradient, it is in the negative $y-$direction.
- In the case where the flow is caused by plate motion without a pressure gradient, the flow profile is linear, with the fluid motion due solely to its viscosity.
- In the case where the motion is caused by both plate motion and pressure gradient, there is no unique flow profile, and we can have motion in both the negative and positive $y-$direction.

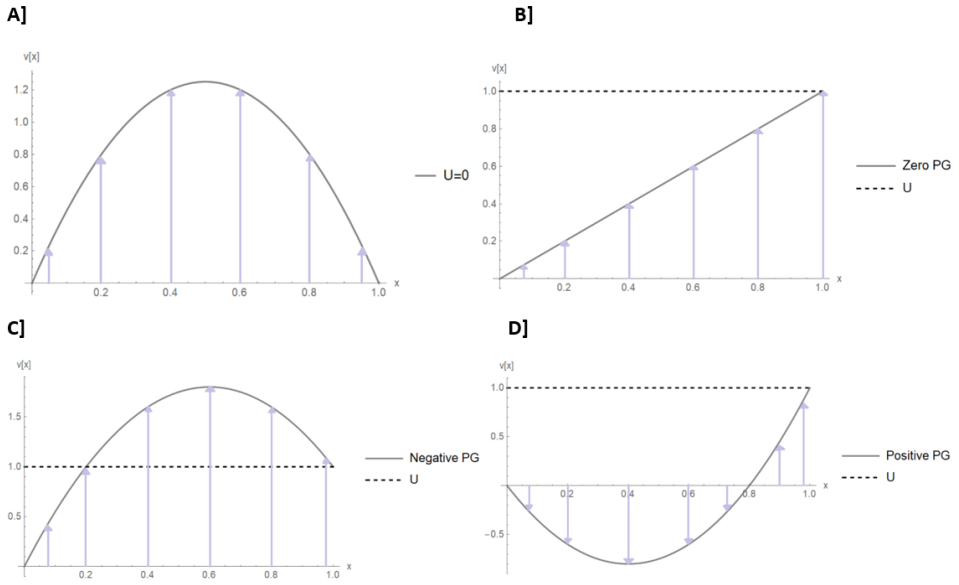

Fig. 2.: [A] Parabolic flow profile, with $U = 0$ and $p_y < 0$. [B] Linear flow profile with $p_y = 0$. [C],[D] Flow due to both plate motion and pressure gradient. In [D] we also observe flow reversal.

2.2. *The Rayleigh flow*

We now proceed to the Rayleigh flow, being an unsteady, incompressible, viscous and two-dimensional flow. The flow takes place over a thin, flat and large plate, which is given a sudden impulse to move in the positive $y-$direction with velocity U. Due to viscosity, fluid motion is generated in the immediate region of the plate, also in the $y-$direction, i.e., as in the *Couette* flow, we have $\mathbf{q} = (0, v(x, y, t), 0)$. We

further assume that there is no pressure gradient. Under these assumptions, the Navier-Stokes equations are reduced to the PDE,

$$\underbrace{v_t = \nu v_{xx}}_{diffusion\ equation}, \ v = v(x,t) \tag{23}$$

with conditions,

$$\begin{cases} v(0,t) = U, \ t > 0, \\ v(\infty,t) = 0, \ t > 0 \end{cases} \tag{24}$$

Applying the well known Laplace transformation, in terms of time t, we obtain,

$$\begin{aligned} & s\mathcal{L}\{v\}(x,s) = \nu \mathcal{L}_{xx}\{v\}(x,s) \\ \Leftrightarrow \ & \mathcal{L}_{xx}\{v\}(x,s) - \frac{s}{\nu}\mathcal{L}\{v\}(x,s) = 0 \\ \Leftrightarrow \ & \mathcal{L}\{v\}(x,s) = A(s)e^{-\frac{x}{\sqrt{\nu}}\sqrt{s}} + B(s)e^{\frac{x}{\sqrt{\nu}}\sqrt{s}} \end{aligned} \tag{25}$$

Furthermore, the boundary conditions are transformed as,

$$\begin{cases} \mathcal{L}\{v\}(0,s) = \dfrac{U}{s}, \\ \\ \mathcal{L}\{v\}(\infty,s) = 0 \end{cases} \tag{26}$$

so (25) becomes,

$$\begin{aligned} & \mathcal{L}\{v\}(x,s) = \frac{U}{s}e^{-\frac{x}{\sqrt{\nu}}\sqrt{s}} \\ \Leftrightarrow \ & v(x,t) = U \operatorname{erfc}\left(\frac{x}{2\sqrt{\nu t}}\right) \\ & = U\left(1 - \underbrace{\frac{2}{\sqrt{\pi}}\int_0^{\eta} e^{-\xi^2} d\xi}_{:=\operatorname{erf}(\eta)}\right), \quad \eta := \frac{x}{2\sqrt{\nu t}} \end{aligned}$$

It is worth noting that the solution is eventually expressed in a similarity solution form,

$$\begin{cases} v(x,t) = Uf(\eta), \\ \eta = \frac{1}{2\sqrt{\nu}} x t^{-\frac{1}{2}} \end{cases} \tag{27}$$

2.3. *The Stokes, oscillatory flow*

In the same framework as in the Rayleigh flow we have the Stokes oscillatory flow,

$$\begin{cases} v_t = \nu v_{xx}, \nu > 0, \\ v(0,t) = U\cos\omega t, \\ v(\infty,t) = 0 \end{cases} \tag{28}$$

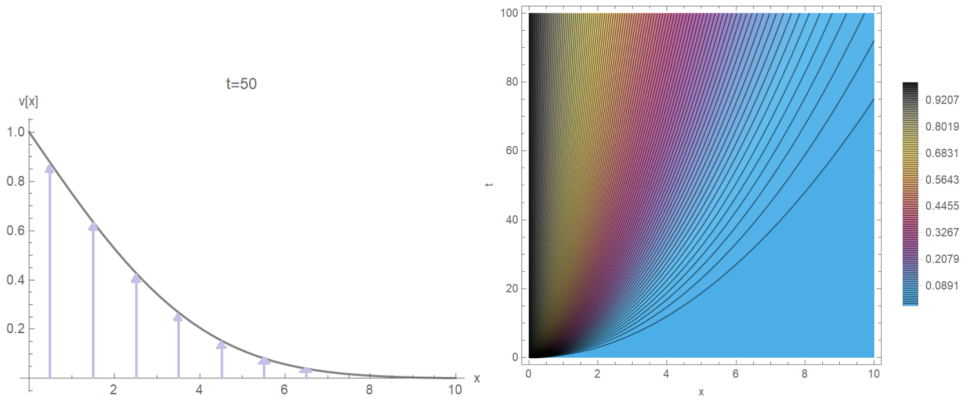

Fig. 3.: Graphic representation of the *Rayleigh* flow, for $\mu = 0.1$ and $U = \rho = 1$. On the left we have a snapshot of the flow profile and on the right contour curves of $v(x,t)$.

Utilizing the transformation,

$$v(x,t) = U\Re\{f(y)e^{i\omega t}\},\ \ f = f_1 + if_2 \tag{29}$$

we are granted with the solution,

$$v(x,t) = U\exp\left(-\sqrt{\frac{\omega}{2\nu}}x\right)\cos\left(\omega t - \sqrt{\frac{\omega}{2\nu}}x\right) \tag{30}$$

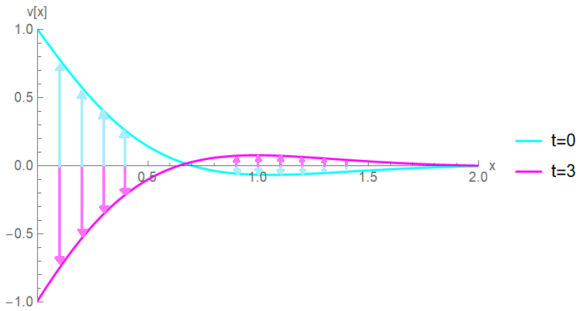

Fig. 4.: Graphical representation of the Stokes oscillatory flow, at two times, for $U = \omega = 1$ and $\nu = 0.1$.

2.4. *The Landau–Squire flow*

In the 1960s, analytical solutions of the NS equations, in their complete form, were found in the two-dimensional case. The problem in three dimensions remains open. In the following, we will discuss two of these analytical solutions, the Landau–Squire

jet and the Taylor–Green vortex. In fluid dynamics, the Landau-Squire flow (or jet) describes a jet emitted from a point source into an infinite fluid medium of the same kind, and is an analytical solution of the incompressible form of the NS equations. We can imagine a quite thin needle injecting some fluid into a large tube filled with the same fluid. The problem is described in spherical coordinates (r, θ, ϕ), with $\mathbf{q} = (u_r, 0, u_\phi)$, with the flow here being axisymmetric, i.e. independent of θ. The point source (needle tip) is located at the origin of the axes, and the fluid is injected in the direction $\phi = 0$. The solution describes a jet of fluid moving rapidly away from the origin, dragging along the slowly moving fluid out of the jet. In spherical coordinates we obtain,

$$\begin{cases} \dfrac{1}{r^2}\dfrac{\partial}{\partial r}(r^2 u_r) + \dfrac{1}{r\sin\phi}\dfrac{\partial}{\partial\phi}(u_\phi \sin\phi) = 0 \\ \\ u_r\dfrac{\partial u_r}{\partial r} + \dfrac{u_\phi}{r}\dfrac{\partial u_r}{\partial\phi} - \dfrac{u_\phi^2}{r} = -\dfrac{1}{\rho}\dfrac{\partial p}{\partial r} + \nu\left(\nabla^2 u_r - \dfrac{2u_r}{r^2} - \dfrac{2}{r^2}\dfrac{\partial u_\phi}{\partial\phi} - \dfrac{2u_\phi\cot\phi}{r^2}\right) \\ \\ u_r\dfrac{\partial u_\phi}{\partial r} + \dfrac{u_\phi}{r}\dfrac{\partial u_\phi}{\partial\phi} + \dfrac{u_r u_\phi}{r} = -\dfrac{1}{\rho r}\dfrac{\partial p}{\partial\phi} + \nu\left(\nabla^2 u_\phi + \dfrac{2}{r^2}\dfrac{\partial u_r}{\partial\phi} - \dfrac{u_\phi}{r^2\sin^2\phi}\right) \end{cases} \tag{31}$$

where,

$$\nabla^2 = \frac{1}{r^2}\frac{\partial}{\partial r}\left(r^2\frac{\partial}{\partial r}\right) + \frac{1}{r^2\sin\phi}\frac{\partial}{\partial\phi}\left(\sin\phi\frac{\partial}{\partial\phi}\right) \tag{32}$$

The solution derived by *Squire*, with stream function $\Psi = \nu r F(\phi)$, which satisfies these equations is,[2]

$$\begin{cases} u_r := \dfrac{\Psi_\phi}{r^2\sin\phi} = \dfrac{\nu F'(\phi)}{r\sin\phi}, \\ \\ u_\phi := -\dfrac{\Psi_r}{r\sin\phi} = -\dfrac{\nu F(\phi)}{r\sin\phi}, \quad , \; F(\phi) = \dfrac{2\sin^2\phi}{1-\cos\phi + C} \\ \\ p = \rho\left(-\dfrac{u_\phi^2}{2} + \dfrac{\nu u_r}{r}\right) \end{cases} \tag{33}$$

The constant C refers to the force at the origin (when the fluid is injected from the tip of the needle), which acts in the direction of the jet.[2]

2.5. *The Taylor–Green Vortex*

The Taylor–Green vortex is also a closed-form analytical solution of the two-dimensional and incompressible form of the Navier–Stokes equations. The two-dimensional decreasing vortex is defined in the rectangle $[0, 2\pi]^2$ and serves (among other things) as a reference problem for testing as well as validating various numerical techniques for solving the incompressible Navier–Stokes equations.[2] The

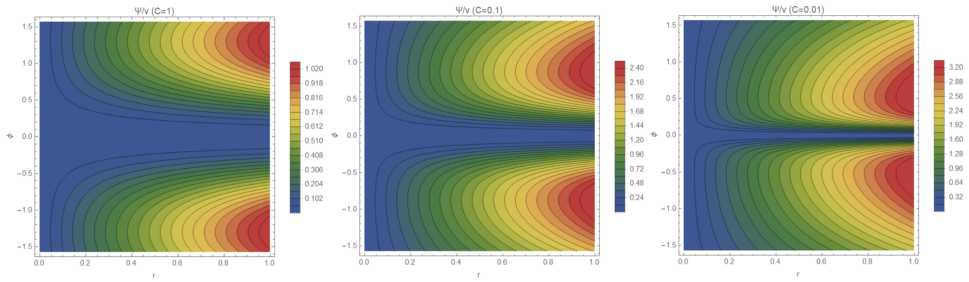

Fig. 5.: Graphic representation of the contour curves of Ψ/ν, for three gradually decreasing values of the constant C.

Taylor–Green vortex, for the incompressible and two–dimensional NS system, in the absence of an external force, is expressed as,[2]

$$\begin{cases} u(x,y) = \cos x \sin y F(t), \\ v(x,y) = -\sin x \cos y F(t) \end{cases} , \; F(t) = e^{-2\nu t} \tag{34}$$

The pressure is obtained by substituting u and v into the equations, as,

$$p(x,y) = -\frac{\rho}{4}\left[\cos(2x) + \cos(2y)\right] F^2(t) \tag{35}$$

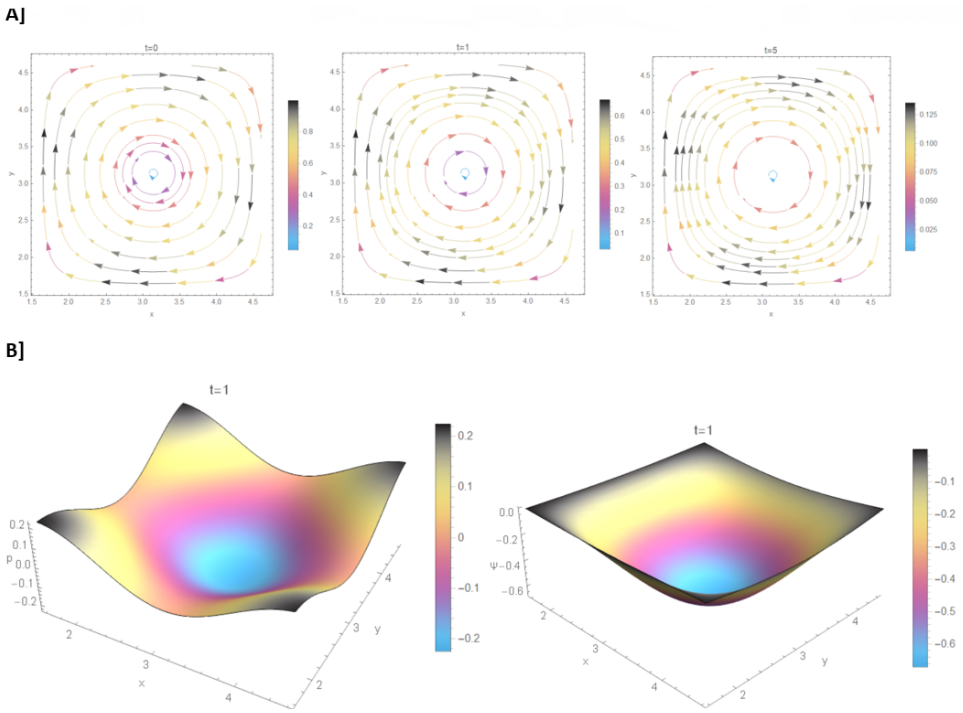

Fig. 6.: [A] Temporal evolution of the Taylor–Green vortex, which as we can see gradually decreases to zero. [B] Graphical representation of the pressure (left) and stream function (right), for $\nu = 0.2$, $\rho = t = 1$.

Two–dimensional FSI methods

3. Two–dimensional FSI methods for the Navier–Stokes equations

In this section, the application of generalized curvilinear coordinates (GCCs) allows the mathematical modeling of complex structures, encountered in Biofluid Dynamics (BFD). Figueroa introduced the coupled momentum method as an advanced fluid-structure interaction (FSI) approach.[6] This methodology enables the description of blood flow in three-dimensional deformable models of arteries. The coupled momentum method incorporates the coupling of the equations for vessel wall deformation with the fluid domain, emphasizing a strong coupling between the degrees of freedom of the fluid and solid domains. Additionally, a linear membrane model is employed for the vessel wall. Building upon this, Quarteroni introduced both three-dimensional and one-dimensional mathematical models to address flow problems in compliant vessels.[8] The fluid transport equations of mass and momentum are transformed into a moving, body–fitted reference frame. FSI numerical studies have been conducted, involving the reconstruction of patient-specific three-dimensional geometries from computed tomography (CT) scans of abdominal aortic aneurysms (AAAs).[18,19] The developed Euler–Lagrange mathematical method distinguishes the interface between fluid flow and the arterial wall. This approach is applicable in many biomedical problems, since the exact position of the fluid–solid interface is of great importance.

3.1. *Dimensionless equations*

We present the fundamental fluid equations, continuity and momentum, describing the pulsatile blood flow in a moving geometry. The governing equations are transformed to a moving body–fitted coordinate system using the generalized curvilinear coordinates (GCCs).[16] Continuity and momentum equations in Cartesian coordinates for a two–dimensional, Newtonian fluid flow can be written in dimensional form as shown in (36)–(38).[15]

continuity equation

$$\frac{\partial \rho}{\partial \tilde{t}} + \frac{\partial(\rho \tilde{u})}{\partial \tilde{x}} + \frac{\partial(\rho \tilde{v})}{\partial \tilde{y}} = 0, \tag{36}$$

x-momentum equation

$$\frac{\partial\left(\rho \tilde{u}\right)}{\partial \tilde{t}} + \frac{\partial\left(\rho \tilde{u} \tilde{u}\right)}{\partial \tilde{x}} + \frac{\partial\left(\rho \tilde{u} \tilde{v}\right)}{\partial \tilde{y}} = -\frac{\partial \tilde{p}}{\partial \tilde{x}} + \left[\frac{\partial}{\partial \tilde{x}}\left(\mu \frac{\partial \tilde{u}}{\partial \tilde{x}}\right) + \frac{\partial}{\partial \tilde{y}}\left(\mu \frac{\partial \tilde{u}}{\partial \tilde{y}}\right)\right], \tag{37}$$

y-momentum equation

$$\frac{\partial(\rho\tilde{v})}{\partial\tilde{t}}+\frac{\partial(\rho\tilde{u}\tilde{v})}{\partial\tilde{x}}+\frac{\partial(\rho\tilde{v}\tilde{v})}{\partial\tilde{y}}=-\frac{\partial\tilde{p}}{\partial\tilde{y}}+\left[\frac{\partial}{\partial\tilde{x}}\left(\mu\frac{\partial\tilde{v}}{\partial\tilde{x}}\right)+\frac{\partial}{\partial\tilde{y}}\left(\mu\frac{\partial\tilde{v}}{\partial\tilde{y}}\right)\right], \tag{38}$$

where $\tilde{u}$ and $\tilde{v}$ are the components of the velocity vector, $\tilde{p}$ is the hydrostatic pressure, ρ is the density, and μ is the viscosity of the fluid. Introducing the dimensionless parameters, equation (39), the system of equations (36)–(38) is transformed to a dimensionless form.

$$x=\frac{\tilde{x}}{R},\;\; y=\frac{\tilde{y}}{R},\;\; t=\frac{\tilde{t}}{R/u_0},\;\; u=\frac{\tilde{u}}{u_0},\;\; \upsilon=\frac{\tilde{v}}{u_0},\;\; p=\frac{\tilde{p}}{\rho u_0^2},\;\; c=\frac{\rho}{\rho_0}, \tag{39}$$

where R is the inlet length of the aneurysmal geometry and u_0 is the characteristic inlet velocity. In this dimensionless form, the continuity equation does not change, while in the momentum equations the Reynolds number is introduced.

continuity equation, dimensionless

$$\frac{\partial c}{\partial t}+\frac{\partial(cu)}{\partial x}+\frac{\partial(cv)}{\partial y}=0, \tag{40}$$

x-momentum equation, dimensionless

$$\frac{\partial u}{\partial t}+\frac{\partial(uu)}{\partial x}+\frac{\partial(uv)}{\partial y}=-\frac{\partial p}{\partial x}+\frac{\partial}{\partial x}\left(\frac{1}{Re}\frac{\partial u}{\partial x}\right)+\frac{\partial}{\partial y}\left(\frac{1}{Re}\frac{\partial u}{\partial y}\right), \tag{41}$$

y-momentum equation, dimensionless

$$\frac{\partial v}{\partial t}+\frac{\partial(uv)}{\partial x}+\frac{\partial(vv)}{\partial y}=-\frac{\partial p}{\partial y}+\frac{\partial}{\partial x}\left(\frac{1}{Re}\frac{\partial v}{\partial x}\right)+\frac{\partial}{\partial y}\left(\frac{1}{Re}\frac{\partial v}{\partial y}\right), \tag{42}$$

where u, v are the dimensionless components of the fluid velocity; p the dimensionless fluid pressure; and Re is the *Reynolds* number, $Re=\dfrac{u_0R}{\nu}$, where ν is the kinematic fluid viscosity.

Applying the generalized curvilinear coordinates (GCCs) transformation, the system of equations (40)–(42) is written in a body–fitted approach. This is possible because there is a local transformation from the physical domain to a normalized one.

The function of the transformation has to be a one–to–one thus ensuring the existence of the inverse. In this approach, the metrics of the transformation, $x_\xi, x_\eta, y_\xi, y_\eta$, can be computed locally, on each finite volume. The determinant of the inverse Jacobian of the transformation for each volume is given by the expression, $J=x_\xi y_\eta - x_\eta y_\xi$. First–order derivatives with respect to x and y for a transport quantity, ϕ, can be written as,

$$\begin{aligned}
\frac{\partial\phi}{\partial x}&=\frac{\partial\phi}{\partial\xi}\frac{\partial\xi}{\partial x}+\frac{\partial\phi}{\partial\eta}\frac{\partial\eta}{\partial x}=\xi_x\frac{\partial\phi}{\partial\xi}+\eta_x\frac{\partial\phi}{\partial\eta}=\frac{y_\eta}{J}\frac{\partial\phi}{\partial\xi}-\frac{y_\xi}{J}\frac{\partial\phi}{\partial\eta},\\
\frac{\partial\phi}{\partial y}&=\frac{\partial\phi}{\partial\xi}\frac{\partial\xi}{\partial y}+\frac{\partial\phi}{\partial\eta}\frac{\partial\eta}{\partial y}=\xi_y\frac{\partial\phi}{\partial\xi}+\eta_y\frac{\partial\phi}{\partial\eta}=-\frac{x_\eta}{J}\frac{\partial\phi}{\partial\xi}+\frac{x_\xi}{J}\frac{\partial\phi}{\partial\eta}.
\end{aligned} \tag{43}$$

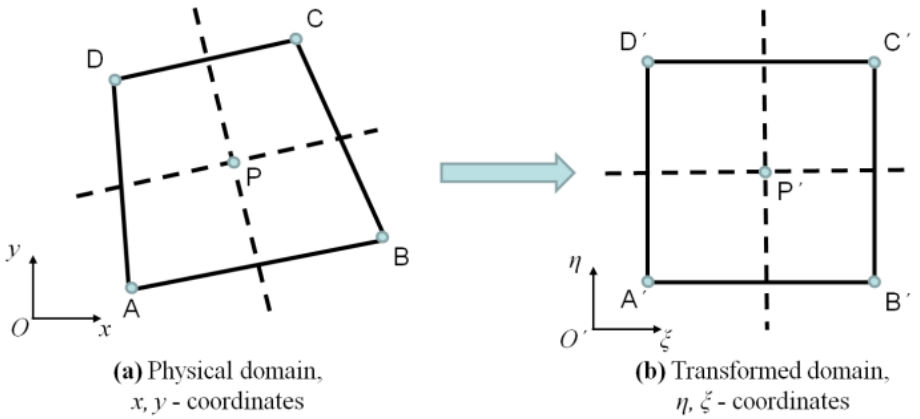

Fig. 7.: The local transformation from the physical to the transformed domain.

Using equation (43), and since the fluid is incompressible, $\rho =$ constant, and $c \simeq 1$ the equations (40)–(42) can be written in curvilinear coordinates, $\xi = \xi(x, y)$, $\eta = \eta(x, y)$, and in dimensionless form as in equations (44)–(46),.[21]

$$\frac{\partial J}{\partial t} + \frac{\partial U}{\partial \xi} + \frac{\partial V}{\partial \eta} = 0, \tag{44}$$

$$\begin{aligned} \frac{\partial (Ju)}{\partial t} + \frac{\partial (Uu)}{\partial \xi} + \frac{\partial (Vu)}{\partial \eta} = & -\left(y_\eta \frac{\partial p}{\partial \xi} - y_\xi \frac{\partial p}{\partial \eta} \right) \\ & + \frac{\partial}{\partial \xi}\left[\frac{1}{JRe}\left(q_1 \frac{\partial u}{\partial \xi} - q_2 \frac{\partial u}{\partial \eta} \right) \right] + \frac{\partial}{\partial \eta}\left[\frac{1}{JRe}\left(q_3 \frac{\partial u}{\partial \eta} - q_2 \frac{\partial u}{\partial \xi} \right) \right], \end{aligned} \tag{45}$$

$$\begin{aligned} \frac{\partial (Jv)}{\partial t} + \frac{\partial (Uv)}{\partial \xi} + \frac{\partial (Vv)}{\partial \eta} = & -\left(x_\xi \frac{\partial p}{\partial \eta} - x_\eta \frac{\partial p}{\partial \xi} \right) \\ & + \frac{\partial}{\partial \xi}\left[\frac{1}{JRe}\left(q_1 \frac{\partial v}{\partial \xi} - q_2 \frac{\partial v}{\partial \eta} \right) \right] + \frac{\partial}{\partial \eta}\left[\frac{1}{JRe}\left(q_3 \frac{\partial v}{\partial \eta} - q_2 \frac{\partial v}{\partial \xi} \right) \right], \end{aligned} \tag{46}$$

Based on the Euler–Lagrange approach, the dimensionless form of the continuity and momentum equations in Cartesian coordinates, equations (40)–(42), are transformed in a body–fitted approach.[3,14] In equations (44)–(46), U and V are the transformed, velocity components defined in equation (47), that takes under consideration the arbitrary motion of the domain; J is the determinant of the inverse Jacobian of the transformation from the physical domain to the normalized one,

$$U = (u - \dot{x})\, y_\eta - (v - \dot{y})\, x_\eta, \;\; V = (v - \dot{y})\, x_\xi - (u - \dot{x})\, y_\xi, \tag{47}$$

where u, v are the fluid velocities and the arbitrary grid motion velocities, $\dot{x}$, $\dot{y}$ are given by a first–order backward difference scheme.[15]

Finally, the quantities q_1, q_2, q_3, entering in equations (44)–(46), are defined as in equation (48),

$$q_1 = x_\eta^2 + y_\eta^2, \;\; q_2 = x_\xi x_\eta + y_\xi y_\eta, \;\; q_3 = x_\xi^2 + y_\xi^2, \tag{48}$$

where, x_ξ, x_η, y_ξ and y_η are the metrics of the transformation that can be computed locally on each finite volume using finite differences. In the arbitrary Euler–Lagrange grid motion, the inverse Jacobian of the transformation, J, is a function of time, and the transformed velocities are functions of the physical u, v fluid velocities and the velocities of the grid motion, $\dot{x}$, $\dot{y}$.[15] Womersley number, a dimensionless expression of the pulsatile flow frequency in relation to the viscous effect, is given by the expression, $Wo = R\sqrt{\frac{\omega}{\nu}}$, where ω is the angular frequency of the pulsations.

3.2. *Boundary and initial conditions*

The introduction of the system of equations that describes blood flow in an aneurysmal geometry in combination with a moving interface, e.g wall, requires a number of specialized boundary conditions. We impose a time–dependent condition for the inlet velocity that describes the pulsatile blood flow in the aneurysmatic vessel during the cardiac cycle, composed of the systolic and diastolic phases. At the outflow, we assume a fully developed flow and that the pressure is known at the outlet. At the center of the fluid domain, we assume symmetry boundary condition. Finally, at the wall, we impose a kinematic boundary condition.

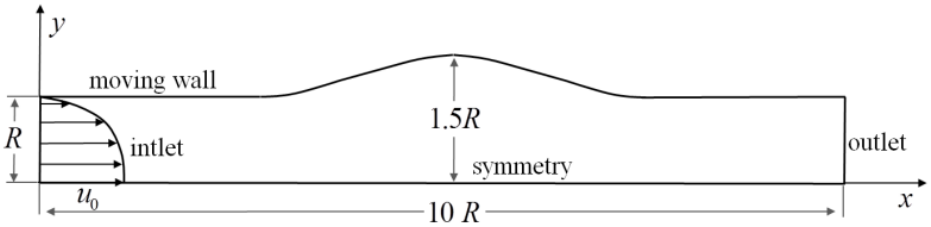

Fig. 8.: An outline of the geometry and the boundary conditions applied on the aneurysmal model[20]

The dimensionless boundary conditions of the equations (44)–(46), are:

- at the inlet, for $t \geq 0$: $u(y,t) = \left[1 - \left(\frac{y}{R}\right)^2\right] \times$ velocity waveform(t), $\upsilon = 0,\ 0 \leqslant y \leqslant R$,
- at the moving wall : $u = \dot{x},\ \upsilon = \dot{y},$ kinematic boundary condition,
- at the symmetry : $\frac{\partial u}{\partial y} = 0,\ \upsilon = 0,$ for $t \geq 0$,
- at the outlet : $p =$ pressure waveform(t), $\frac{\partial u}{\partial x} = 0,\ \frac{\partial \upsilon}{\partial x} = 0,$ fully developed flow assumption.

Velocity and pressure waveforms are extracted from the literature[12] and are fitted

with Fourier series.[11]

For the numerical solution of the system of equations (44)–(46) subject to the boundary conditions, a numerical Euler–Lagrange technique is developed. In this technique, the finite volume method was used for discretizing the nonlinear set of equations. For the numerical solution of the problem we utilize a direct numerical approach and a numerical program is developed in MATLAB (MathWorks, Natick, MA, USA). The system of equations is written in dimensionless form to simplify the numerical calculations needed for the numerical solution.

3.3. *Finite volume discretization method*

The proposed finite volume method has second–order accuracy for the spatial derivatives in the fluid domain and first–order accuracy for the time derivative, leading to an implicit scheme.[1,5,7] The upwind scheme is further introduced to the discretized equations to overcome problems concerning high convection terms in the momentum. With this formulation, the convective terms obtain first–order accuracy, and their influence is minimized, while the diffusion terms remain unchanged (second–order accuracy) as the velocity increases in the flow field. Additionally, we could use higher–order upwind schemes or the power law scheme.[7] The discretized form of equations (49)–(51) with the finite volume approach is shown below:

$$\frac{J-J_0}{\Delta t}+U_e-U_w+V_n-V_s=0, \tag{49}$$

$$\frac{Ju-J_0u_0}{\Delta t}+\left[Uu-\frac{1}{J\,\mathrm{Re}}\left(q_1\frac{\partial u}{\partial \xi}-q_2\frac{\partial u}{\partial \eta}\right)+\frac{\partial y}{\partial \eta}p\right]_e-\left[Uu-\frac{1}{J\,\mathrm{Re}}\left(q_1\frac{\partial u}{\partial \xi}-q_2\frac{\partial u}{\partial \eta}\right)+\frac{\partial y}{\partial \eta}p\right]_w$$
$$+\left[Vu-\frac{1}{J\,\mathrm{Re}}\left(-q_2\frac{\partial u}{\partial \xi}+q_3\frac{\partial u}{\partial \eta}\right)-\frac{\partial y}{\partial \xi}p\right]_n-\left[Vu-\frac{1}{J\,\mathrm{Re}}\left(-q_2\frac{\partial u}{\partial \xi}+q_3\frac{\partial u}{\partial \eta}\right)-\frac{\partial y}{\partial \xi}p\right]_s=0, \tag{50}$$

$$\frac{Jv-J_0v_0}{\Delta t}+\left[Uv-\frac{1}{J\,\mathrm{Re}}\left(q_1\frac{\partial v}{\partial \xi}-q_2\frac{\partial v}{\partial \eta}\right)+\frac{\partial x}{\partial \eta}p\right]_e-\left[Uv-\frac{1}{J\,\mathrm{Re}}\left(q_1\frac{\partial v}{\partial \xi}-q_2\frac{\partial v}{\partial \eta}\right)+\frac{\partial x}{\partial \eta}p\right]_w$$
$$+\left[Vv-\frac{1}{J\,\mathrm{Re}}\left(-q_2\frac{\partial v}{\partial \xi}+q_3\frac{\partial v}{\partial \eta}\right)-\frac{\partial x}{\partial \xi}p\right]_n-\left[Vv-\frac{1}{J\,\mathrm{Re}}\left(-q_2\frac{\partial v}{\partial \xi}+q_3\frac{\partial v}{\partial \eta}\right)-\frac{\partial x}{\partial \xi}p\right]_s=0, \tag{51}$$

where the subscript 0 refers to the previous time level, and the subscripts e, w, n, s are refereed to the four faces of each finite volume. The Cartesian components of the mesh velocity vector, $(\dot{x}, \dot{y})$, are approximated by a first–order backward difference scheme.[14]

The velocity field is visually depicted in **Figure 10(a)**, while **Figure 10(b)** illustrates the pressure distribution of the viscous fluid at four different time points of the cardiac cycle. Due to viscous forces, pulsatile boundary conditions, and a large Womersley number, the velocity experiences drastic changes downstream from the aneurysmal structure, resulting in a plug-like profile. The inflow velocity is considered parabolic and pulsatile, as depicted in **Figure 8**. The pulsating aortic wall

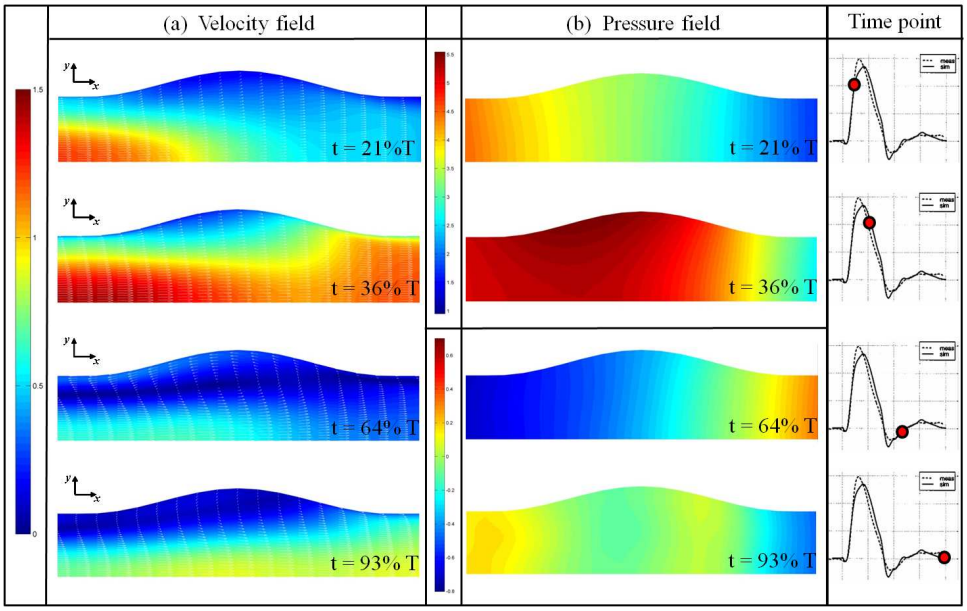

Fig. 9.: (a) Fluid velocity field at four different time points during the cardiac cycle. (b) Pressure is presented at the same time points during the cardiac cycle, adopted from[20]

tissue significantly influences the velocity field, leading to intensified flow patterns compared to simulations with a static wall.

The pressure distribution generated by the dynamic blood flow patterns during the cardiac cycle within the aneurysm contributes significantly to increased wall stresses and exacerbates the risk of rupture. The results highlight that the highest dimensionless pressure, denoted as p, and the greatest pressure drop, represented by Δp, occur during systole. The pressure drop refers to the pressure difference between the inlet and outlet. During systole, the pressure drop remains relatively high and reduces significantly during the diastolic phase. The pressure field exhibits areas of lateral pressure gradient, particularly in the aneurysmal region, especially noticeable during diastole, indicating significant disturbances in the flow field. The interested reader could find more details in.[15]

Three–dimensional FSI methods

4. A generalization to three–dimensional FSI methods

In this section, focus is set on generalizing the already presented two-dimensional FSI methods to higher-dimensional flows. As previously seen, the dimensionless form of the Navier–Stokes equations, for an incompressible flow, in time and space, is expressed as (in closed form),

$$\begin{cases} u_x + v_y + w_z = 0, \\ \\ u_t + (u^2)_x + (vu)_y + (wu)_z = -p_x + \dfrac{1}{Re}\left(u_{xx} + u_{yy} + u_{zz}\right), \\ \\ v_t + (uv)_x + (v^2)_y + (wv)_z = -p_y + \dfrac{1}{Re}\left(v_{xx} + v_{yy} + v_{zz}\right), \\ \\ w_t + (uw)_x + (vw)_y + (w^2)_z = -p_z + \dfrac{1}{Re}\left(w_{xx} + w_{yy} + w_{zz}\right) \end{cases} \tag{52}$$

The above set of equations is already casted into a conservative form, suitable for numerical treatment, and reads,

$$\begin{cases} \boldsymbol{\nabla} \cdot \overline{q} = 0, \quad \overline{q} = (u, v, w), \\ \overline{q}_{i_t} + \boldsymbol{\nabla} \cdot \left(\overline{q}_i \overline{q} + p \cdot \overline{e}_i - \dfrac{1}{Re} \boldsymbol{\nabla} \overline{q}_i \right) = \overline{0} \end{cases} \quad , \ i = 1, 2, 3, \ e_i : \ \textit{standard basis of } \mathbb{R}^3. \tag{53}$$

Here, same as in the formerly seen two-dimensional setting, it is assumed that there is a unique and invertible relation between the transformed (normalized) and the physical coordinates, expressed as,

$$\begin{cases} \xi = \xi(x, y, z), \\ \eta = \eta(x, y, z), \\ \zeta = \zeta(x, y, z) \end{cases} \tag{54}$$

with the inverse relation being,

$$\begin{cases} x = x(\xi, \eta, \zeta), \\ y = y(\xi, \eta, \zeta), \\ z = z(\xi, \eta, \zeta) \end{cases} \tag{55}$$

The Jacobian matrix of the transformation (54) is given by,

$$J = \begin{bmatrix} \xi_x & \xi_y & \xi_z \\ \eta_x & \eta_y & \eta_z \\ \zeta_x & \zeta_y & \zeta_z \end{bmatrix} \tag{56}$$

whereas the one of the inverse transformation (55) by,

$$J^{-1} = \begin{bmatrix} x_\xi & x_\eta & x_\zeta \\ y_\xi & y_\eta & y_\zeta \\ z_\xi & z_\eta & z_\zeta \end{bmatrix} \tag{57}$$

The determinant of J^{-1} is expressed as,

$$|J^{-1}| = x_\xi \left(y_\eta z_\zeta - y_\zeta z_\eta\right) + x_\eta \left(z_\xi y_\zeta - y_\xi z_\zeta\right) + x_\zeta \left(y_\xi z_\eta - z_\xi y_\eta\right). \tag{58}$$

Therefore, one obtains,

$$\begin{aligned} J &= (J^{-1})^{-1} \\ &= \frac{1}{|J^{-1}|} \begin{bmatrix} y_\eta z_\zeta - z_\eta y_\zeta & x_\zeta z_\eta - z_\zeta x_\eta & x_\eta y_\zeta - y_\eta x_\zeta \\ y_\zeta z_\xi - z_\zeta y_\xi & x_\xi z_\zeta - z_\xi x_\zeta & x_\zeta y_\xi - y_\zeta x_\xi \\ y_\xi z_\eta - z_\xi y_\eta & x_\eta z_\xi - z_\eta x_\xi & x_\xi y_\eta - y_\xi x_\eta \end{bmatrix}. \end{aligned} \tag{59}$$

Finally, defining,

$$\begin{cases} \overline{q} = (u, v, w), \\ \overline{q_r} = (u - \dot{x}, v - \dot{y}, w - \dot{z}), \\ \overline{q} = (U, V, W) = |J^{-1}| q_r J. \end{cases} \tag{60}$$

The physical velocities, u, v and w are transformed to U, V and W, being the contravariant velocity components, considering the arbitrary motion of the domain. Moreover, the arbitrary grid motion velocities, $\dot{x}$, $\dot{y}$ and $\dot{z}$ are obtained numerically.[15] Considering an incompressible fluid motion, driven by a pressure p, the dimensionless continuity equation reads,

$$\left(\rho |J^{-1}|\right)_t + \boldsymbol{\nabla}_g \cdot (\rho \overline{q}) = 0, \quad \boldsymbol{\nabla}_g := \left(\frac{\partial}{\partial \xi}, \frac{\partial}{\partial \eta}, \frac{\partial}{\partial \zeta}\right) \tag{61}$$

whereas the Navier–Stokes momentum equations are given as,

$$\left(\overline{q}_i |J^{-1}|\right)_t + \boldsymbol{\nabla}_g \cdot \left(\overline{q}_i \overline{q} - \frac{1}{Re |J^{-1}|} \boldsymbol{\nabla}_g \overline{q}_i Q + |J^{-1}| p J_i\right) = \overline{0}, \quad i = 1, 2, 3. \tag{62}$$

Here, Re, stands for the dimensionless Reynolds number,[20] whereas J_i stands for the i-th column of J. Finally,

$$Q = |J^{-1}|^2 \begin{bmatrix} |\boldsymbol{\nabla}\xi|^2 & \boldsymbol{\nabla}\xi \cdot \boldsymbol{\nabla}\eta & \boldsymbol{\nabla}\xi \cdot \boldsymbol{\nabla}\zeta \\ \boldsymbol{\nabla}\eta \cdot \boldsymbol{\nabla}\xi & |\boldsymbol{\nabla}\eta|^2 & \boldsymbol{\nabla}\eta \cdot \boldsymbol{\nabla}\zeta \\ \boldsymbol{\nabla}\zeta \cdot \boldsymbol{\nabla}\xi & \boldsymbol{\nabla}\zeta \cdot \boldsymbol{\nabla}\eta & |\boldsymbol{\nabla}\zeta|^2 \end{bmatrix}, \quad \boldsymbol{\nabla} := \left(\frac{\partial}{\partial x}, \frac{\partial}{\partial y}, \frac{\partial}{\partial z}\right) \tag{63}$$

Notice that the above formulae generalize the ones presented in the two-dimensional approach.

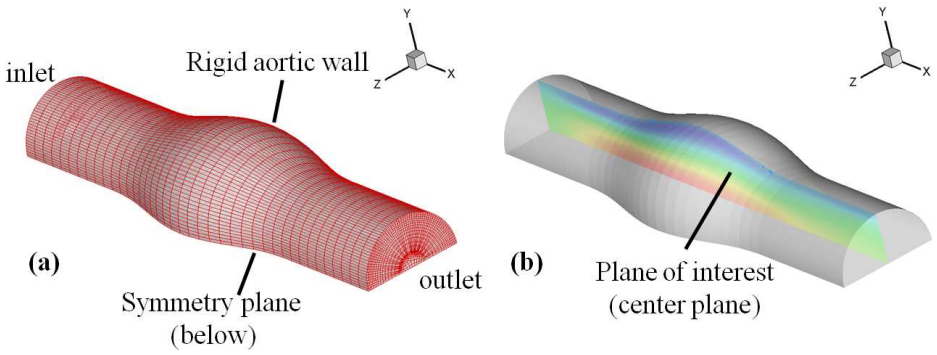

Fig. 10.: A $3D$ model of an aneurysmal artery. (a) Grid. (b) Flow, adopted from[20]

One important aspect of the three–dimensional ($3D$) models is that they can simulate real geometries. Such simulations have the potential to improve the understanding and prediction of rupture locations in aortic aneurysms. This valuable knowledge can assist healthcare professionals in making informed clinical decisions and devising effective treatment strategies for patients afflicted by this condition.

Furthermore, the development of a three-dimensional, solver would enable more accurate and detailed simulations of fluid–structure interactions within the human body. Three–dimensional models of arteries reconstructed from medical imaging data can achieve more realistic and accurate results in studying the complex interactions between fluid flow and the structural behavior of blood vessels.

5. Conclusions

The first section of the study introduced fundamental concepts of fluid mechanics, providing a basis for understanding the subsequent topics. In the second section of this chapter, analytical solutions were presented as exact models to evaluate and validate numerical solvers. Then the focus lies on advanced fluid–structure interaction (FSI) simulations to investigate the behavior of arterial vessels by capturing the dynamic interaction between vessel hemodynamics and wall deformation. The focus was specifically on utilizing two–dimensional FSI methods based on the Navier–Stokes equations to model blood flow in arteries mathematically. The obtained cardiovascular data were rigorously compared with numerical results obtained from numerical methods, establishing the reliability and accuracy of the FSI approach. To comprehensively analyze blood flow throughout the entire cardiac cycle, the initial fluid equations were expanded to a mixed Euler–Lagrange formulation within the FSI framework. Furthermore, transport equations were transformed into a moving body–fitted reference frame using generalized curvilinear coordinates, enhancing the accuracy of the simulations. Additionally, the study introduced and discussed a generalization of the FSI approach to a three–dimensional setting, allowing for

more comprehensive analyses. These findings contribute to a deeper understanding of arterial biomechanics and hold significant implications for the advancement of cardiovascular simulations and treatments.

Acknowledgment:

This research was partially supported by project "Dioni: Computing Infrastructure for Big-Data Processing and Analysis" (MIS No. 5047222) co-funded by European Union (ERDF) and Greece through Operational Program "Competitiveness, Entrepreneurship and Innovation", NSRF 2014-2020.

References

1. Barth, T., Ohlberger, M.: Finite volume methods: foundation and analysis (2003)
2. Batchelor, C.K., Batchelor, G.K.: An introduction to fluid dynamics. Cambridge university press (1967)
3. Braaten, M., Shyy, W.: A study of recirculating flow computation using body-fitted coordinates: consistency aspects and mesh skewness. Numerical Heat Transfer, Part A: Applications **9**(5), 559–574 (1986)
4. Fefferman, C.L.: Existence and smoothness of the navier-stokes equation. The millennium prize problems **57**, 67 (2000)
5. Ferziger, J.H., Perić, M., Street, R.L.: Computational methods for fluid dynamics, vol. 3. Springer (2002)
6. Figueroa, C.A., Vignon-Clementel, I.E., Jansen, K.E., Hughes, T.J., Taylor, C.A.: A coupled momentum method for modeling blood flow in three-dimensional deformable arteries. Computer methods in applied mechanics and engineering **195**(41-43), 5685–5706 (2006)
7. Fletcher, C.A., Fletcher, C.A.: Fluid dynamics: the governing equations. Computational Techniques for Fluid Dynamics 2: Specific Techniques for Different Flow Categories pp. 1–46 (1991)
8. Formaggia, L., Gerbeau, J.F., Nobile, F., Quarteroni, A.: On the coupling of 3d and 1d navier–stokes equations for flow problems in compliant vessels. Computer methods in applied mechanics and engineering **191**(6-7), 561–582 (2001)
9. Kim, S., Karrila, S.J.: Microhydrodynamics: principles and selected applications. Courier Corporation (2013)
10. Ladyzhenskaya, O.A.: The mathematical theory of viscous incompressible flow. Gordon & Breach (1969)
11. Linninger, A.A., Xenos, M., Zhu, D.C., Somayaji, M.R., Kondapalli, S., Penn, R.D.: Cerebrospinal fluid flow in the normal and hydrocephalic human brain. IEEE Transactions on Biomedical Engineering **54**(2), 291–302 (2007)
12. Olufsen, M.S., Peskin, C.S., Kim, W.Y., Pedersen, E.M., Nadim, A., Larsen, J.: Numerical simulation and experimental validation of blood flow in arteries with structured-tree outflow conditions. Annals of biomedical engineering **28**, 1281–1299 (2000)
13. Patankar, S.: Numerical heat transfer and fluid flow. Taylor & Francis (2018)
14. Shyy, W., Tong, S.S., Correa, S.M.: Numerical recirculating flow calculation using a body-fitted coordinate system. Numerical Heat Transfer **8**(1), 99–113 (1985)

15. Shyy, W., Udaykumar, H., Rao, M.M., Smith, R.W.: Computational fluid dynamics with moving boundaries. Courier Corporation (2012)
16. Thompson, J.F., Warsi, Z.U., Mastin, C.W.: Numerical grid generation: foundations and applications. Elsevier North-Holland, Inc. (1985)
17. Vignon-Clementel, I.E., Figueroa, C.A., Jansen, K.E., Taylor, C.A.: Outflow boundary conditions for three-dimensional finite element modeling of blood flow and pressure in arteries. Computer methods in applied mechanics and engineering **195**(29-32), 3776–3796 (2006)
18. Xenos, M., Alemu, Y., Zamfir, D., Einav, S., Ricotta, J.J., Labropoulos, N., Tassiopoulos, A., Bluestein, D.: The effect of angulation in abdominal aortic aneurysms: fluid–structure interaction simulations of idealized geometries. Medical & biological engineering & computing **48**, 1175–1190 (2010)
19. Xenos, M., Rambhia, S.H., Alemu, Y., Einav, S., Labropoulos, N., Tassiopoulos, A., Ricotta, J.J., Bluestein, D.: Patient-based abdominal aortic aneurysm rupture risk prediction with fluid structure interaction modeling. Annals of biomedical engineering **38**, 3323–3337 (2010)
20. Xenos, M.A.: An euler–lagrange approach for studying blood flow in an aneurysmal geometry. Proceedings of the Royal Society A: Mathematical, Physical and Engineering Sciences **473**(2199), 20160,774 (2017)
21. Zhang, L., Kulkarni, K., Somayaji, M.R., Xenos, M., Linninger, A.A.: Discovery of transport and reaction properties in distributed systems. AIChE Journal **53**(2), 381–396 (2007)